

A RIGOROUS FOREST SCATTERING MODEL VALIDATION THROUGH COMPARISON WITH INDOOR BISTATIC SCATTERING MEASUREMENTS

S. Bellez^{1,*}, H. Roussel¹, C. Dahon¹, and J. M. Geffrin²

¹UPMC Univ Paris 06, UR2 L2E, Paris F-75252, France

²Institut Fresnel UMR CNRSTIC 6133, Université de Provence, Aix-Marseille I, Université Paul Cézanne, Aix-Marseille III, Ecole Généraliste d'Ingénieurs de Marseille, Campus de Saint-Jerome, Case 162, Marseille Cedex 20 13397, France

Abstract—In this paper, we present numerical simulations and indoor bistatic scattering measurements on scaled targets. The targets are vertical and/or tilted dielectric parallelepipeds representing the main forest elements (tree-trunks and primary branches) at VHF and low-UHF frequencies. They are placed above an aluminum circular plate to simulate a flat ground. The measurements have been conducted in the anechoic chamber of the “Centre Commun de Ressources Micro-ondes” (CCRM) in Marseille, France. A 3D forest scattering model using a Method of Moments (MoM) is deployed to simulate the electric fields scattered by these targets. Two radar geometric, azimuthal and zenithal, bistatic configurations with special attention to the specular direction have been considered. Simulation results and experimental data are confronted for both VV - and HH -polarizations in order to evaluate the accuracy of our model. We have obtained a very good agreement between theoretical and experimental scattered fields for both the magnitude and phase.

1. INTRODUCTION

Studies of bistatic scattering by forested areas have a practical importance for both military and civil remote sensing applications. These studies mainly interested militaries in precise target location or receiver camouflage. They are very useful as well for remote sensing applications like higher accuracy forest parameter estimation

Received 30 June 2011, Accepted 19 July 2011, Scheduled 24 July 2011

* Corresponding author: Sami Bellez (sami.bellez@upmc.fr).

and target detection. Furthermore, bistatic radar configurations are very attractive for interferometric studies [1, 2].

Bistatic radar configurations have a number of attractive benefits but have received only little attention because they are more difficult to handle than conventional monostatic radar configurations [3, 4]. Because of their complexity, outdoor experimental investigations are fairly limited. One of them is the jointly air-borne experiment organized by the German Aerospace Center (Deutsches Zentrum für Luft- und Raumfahrt — DLR) and the French Aerospace Research Establishment (Office National d’Etudes et de Recherches Aérospatiales — ONERA) involving their radar systems E-SAR and RAMSES, respectively [5]. Other fully polarimetric radar scattering measurement of forested hills conducted at large bistatic angles and grazing incidence is reported in [6].

Interest in bistatic radar configurations where the transmitter and the receiver are located on two separate platforms has led to the development of bistatic forest scattering models. They can be classified into two groups. The first group contains the approximate scattering models that are usually based on Radiative Transfer (RT) theory [7] and Distorted Born Approximation (DBA) [8]. The DBA models incorporate the coherence effects associated with target positions while RT models ignore the phase information. The second group includes the rigorous scattering models employing numerical techniques, such as the Method of Moments (MoM) [9, 10] or the Finite-Difference Time-Domain (FDTD) [11], that basically transform integral or integro-differential formulations into a linear system of equations. This kind of models compute the “exact” scattered field at any point above the soil. Theoretical bistatic scattering models have been developed to support the design of experiments and the understanding of the mechanisms involved in the scattering process. A validated scattering model is useful for the retrieval of forest parameters and for classification studies.

Conversely to outdoor measurements, indoor bistatic experiments seem to be more appropriate in testing and validating the developed scattering models. Due to the indoor conditions, environmental variations as well as experimental uncertainties (i.e., antennas positions) are well-controlled and target position is known with high accuracy. Therefore, the experiment parameters can be precisely employed as inputs for the model.

In the last 10 years, various indoor measurements have been conducted in anechoic chambers to characterize the bistatic scattering by canonical and complex targets. Some experiments have been performed by using two antennas on separate platforms [12–16]

while others are carried out with a monostatic radar and a reflective plane [17]. Within this framework, ONERA has performed scaled-model measurements in its anechoic facility BABI. These measurements have served to study electromagnetic wave propagation in forested areas [18] as well as polarimetric scattering by forests in bistatic radar configurations [19].

In this paper, we propose scaled-model measurements in order to validate a 3D rigorous scattering model that simulates the interaction of VHF and low-UHF electromagnetic waves with a forest. This model, based on an electric field volume integral formulation, computes the “exact” scattered field by the forest at any observation point above the soil. Beside that, the model also provides the contribution of the various scattering mechanisms. A MoM with a point matching as testing functions is applied to solve the Electric Field Integral Equation (EFIE). The practical limitation of our approach is related to the available computer memory space, which depends on the frequency of the incident wave and the number of scatterers as well as their sizes. Therefore, our modeling tool doesn’t provide the exact scattering solution for a large number of trees at VHF and UHF-bands. However, for forests having a weak or moderate tree density, the multiple scattering interactions between trees (direct interactions and via the ground) can be ignored and trees can be considered to be independent. That way, the forest response can be reduced to the coherent addition of the fields scattered by each tree. Consequently, the required memory size is reduced and it no longer depends on trees number. In this work, we study the scattering by simplified targets in order to validate our model which can be easily generalized to a natural forest.

The experiments have been conducted on reduced-scale models in the anechoic chamber of the “Centre Commun de Ressources Micro-ondes” (CCRM) in Marseille, France. The forest scale models are composed of an aluminum circular plate, vertical and/or tilted dielectric parallelepipeds respectively representing the forest ground, tree-trunks and/or the primary branches.

The paper is organized as follows: Section 2 briefly describes the theoretical model, including the geometrical representation of the forest, the model formulation and the computation process. In Section 3, we present the indoor scaled-model measurements. This section describes the anechoic chamber of the CCRM, followed with a description of the measured forest scale models. It ends with the measurement steps and the calibration procedure. In Section 4, we compare experimental and theoretical results, then we show the contribution of each scattering mechanism to the scattered field.

2. THE THEORETICAL MODEL

Microwave radar frequencies do not provide useful information on hidden elements of the forest since the wave is strongly attenuated and most forest response originates from the upper canopy layers. However, radar remote sensing of forested areas is preferable at VHF and low-UHF frequencies because of their canopy penetration ability and their sensitivity to many forest parameters. In the following, an electromagnetic formulation provides the scattered field by a simplified geometrical representation of the forest is presented.

2.1. Forest Geometrical Representation

As we consider VHF and low-UHF frequencies, the forest medium doesn't need to be described in detail because at these frequencies waves cannot sense the forest smallest elements. The effects of leaves, needles and the roughness of the soil can be ignored because their contribution is negligible. Hence, the complex geometry of the forest can be reduced to dielectric vertical and tilted cylinders of square cross section (parallelepipeds), representing respectively tree-trunks and primary branches, above a horizontal interface separating two semi-infinite homogeneous media, the air and the soil (see Figure 1(a)).

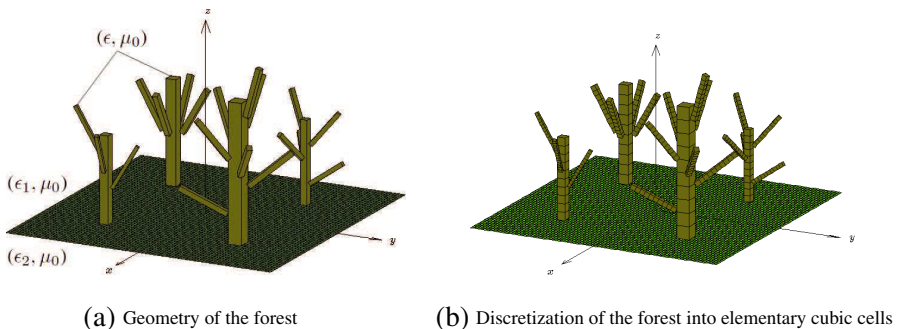


Figure 1. Geometry of the forest and its discretization into elementary cubic cells. $\epsilon_1 = \epsilon_0$, ϵ_2 and ϵ are respectively the free space, ground and wood permittivities, and μ_0 is the free space permeability.

2.2. Model Formulation and Computation Process

A variety of techniques have been developed to characterize electromagnetic scattering by forested areas. In this subsection, we apply an electric field volume integral equation formulation which is

derived from Maxwell's equations. This formulation is well suited to solve scattering problems of inhomogeneous bodies. The volume integral equation is discretized into a linear system of equations by using a MoM. It is then approximated by a matrix equation where unknowns are expressed in terms of internal field inside the trees. The tree-trunks and the main branches are divided into elementary cubic cells which are small enough so that the internal field is nearly uniform in each cell (see Figure 1(b)).

The volume integral equation formulation can also be interpreted to extract the three physical scattering mechanisms: the Simple-bounce (Sb), the Double-bounce (Db), and the Triple-bounce scattering mechanism (Tb). Further details on these scattering mechanisms are reported in [20].

In general, the computation process of the scattered field by the forest can be decomposed into four steps. In the first step, we compute the incident field as well as the one reflected on the ground at the positions of cells discretizing the trees (those fields are computed in the air in absence of the trees). The ground is supposed to be a plane interface, so that the reflection is only in the specular direction. In the second step, we determine the internal field inside the trees, taking into account all interactions (with the use of the dyadic Green's function). The internal field inside the cells of the trees is separated into two parts: one part corresponding to the direct incident wave and the other represents the wave reflected on the ground. Therefore, in order to obtain the two parts of the internal field, we have to solve the two following integral equations (with a MoM method) by considering observation points inside the trees $\bar{\mathbf{r}} \in \Omega$:

$$\bar{\mathbf{E}}_1^t(\bar{\mathbf{r}}) = \bar{\mathbf{E}}^i(\bar{\mathbf{r}}) + (k_0^2 + \nabla\nabla\cdot) \int_{\Omega} \chi(\bar{\mathbf{r}}') \underline{\mathbf{G}}(\bar{\mathbf{r}}, \bar{\mathbf{r}}') \bar{\mathbf{E}}_1^t(\bar{\mathbf{r}}') d\bar{\mathbf{r}}' \quad (1)$$

$$\bar{\mathbf{E}}_2^t(\bar{\mathbf{r}}) = \bar{\mathbf{E}}^r(\bar{\mathbf{r}}) + (k_0^2 + \nabla\nabla\cdot) \int_{\Omega} \chi(\bar{\mathbf{r}}') \underline{\mathbf{G}}(\bar{\mathbf{r}}, \bar{\mathbf{r}}') \bar{\mathbf{E}}_2^t(\bar{\mathbf{r}}') d\bar{\mathbf{r}}' \quad (2)$$

where

- $\bar{\mathbf{E}}^i(\bar{\mathbf{r}})$: incident electric field
- $\bar{\mathbf{E}}^r(\bar{\mathbf{r}})$: reflected electric field on the ground
- $\bar{\mathbf{E}}_1^t(\bar{\mathbf{r}}')$: first part of the internal field induced by $\bar{\mathbf{E}}^i(\bar{\mathbf{r}})$
- $\bar{\mathbf{E}}_2^t(\bar{\mathbf{r}}')$: second part of the internal field induced by $\bar{\mathbf{E}}^r(\bar{\mathbf{r}})$
- $\underline{\mathbf{G}}(\bar{\mathbf{r}}, \bar{\mathbf{r}}')$: dyadic Green's function of two layered media
- $\chi(\bar{\mathbf{r}}') = \frac{\epsilon(\bar{\mathbf{r}}) - \epsilon_0}{\epsilon_0}$: permittivity contrast
- Ω : domain occupied by the trees

- k_0 : free space wavenumber

In the third step, we compute the contributions of the various scattering mechanisms. It should be noticed that the dyadic Green's function is the sum of two parts. The first part is the free space Green's function, $\underline{\mathbf{G}}^s(\bar{\mathbf{r}}, \bar{\mathbf{r}}')$, and the second corresponds to the contribution of the ground called the regular part of the Green's function, $\underline{\mathbf{G}}^r(\bar{\mathbf{r}}, \bar{\mathbf{r}}')$. It is therefore possible to determine the scattered field relied to each scattering mechanism by means of the following equations:

$$\bar{\mathbf{E}}_{\text{Sb}}^s(\bar{\mathbf{r}}) = (k_0^2 + \nabla\nabla\cdot) \int_{\Omega} \chi(\bar{\mathbf{r}}') \underline{\mathbf{G}}^s(\bar{\mathbf{r}}, \bar{\mathbf{r}}') \bar{\mathbf{E}}_1^t(\bar{\mathbf{r}}') d\bar{\mathbf{r}}' \quad (3)$$

$$\bar{\mathbf{E}}_{\text{Db1}}^s(\bar{\mathbf{r}}) = (k_0^2 + \nabla\nabla\cdot) \int_{\Omega} \chi(\bar{\mathbf{r}}') \underline{\mathbf{G}}^s(\bar{\mathbf{r}}, \bar{\mathbf{r}}') \bar{\mathbf{E}}_2^t(\bar{\mathbf{r}}') d\bar{\mathbf{r}}' \quad (4)$$

$$\bar{\mathbf{E}}_{\text{Db2}}^s(\bar{\mathbf{r}}) = (k_0^2 + \nabla\nabla\cdot) \int_{\Omega} \chi(\bar{\mathbf{r}}') \underline{\mathbf{G}}^r(\bar{\mathbf{r}}, \bar{\mathbf{r}}') \bar{\mathbf{E}}_1^t(\bar{\mathbf{r}}') d\bar{\mathbf{r}}' \quad (5)$$

$$\bar{\mathbf{E}}_{\text{Tb}}^s(\bar{\mathbf{r}}) = (k_0^2 + \nabla\nabla\cdot) \int_{\Omega} \chi(\bar{\mathbf{r}}') \underline{\mathbf{G}}^r(\bar{\mathbf{r}}, \bar{\mathbf{r}}') \bar{\mathbf{E}}_2^t(\bar{\mathbf{r}}') d\bar{\mathbf{r}}' \quad (6)$$

The coherent sum of Db1 and Db2 contributions gives the Db scattering mechanism:

$$\bar{\mathbf{E}}_{\text{Db}}^s(\bar{\mathbf{r}}) = \bar{\mathbf{E}}_{\text{Db1}}^s(\bar{\mathbf{r}}) + \bar{\mathbf{E}}_{\text{Db2}}^s(\bar{\mathbf{r}}) \quad (7)$$

It is also important to note that the regular part of the Green's function is obtained by using the Leading-Order Approximation reported in [21]. This approximation reduces the computation time and is valid in our case given that we calculate the scattered fields in the far field zone. Conversely, in the calculation of the internal field, this part is computed using a 2-D Fast Fourier transform algorithm to consider the near field interactions.

In the last step, we need to sum the scattering mechanisms coherently in order to obtain the scattered field by the illuminated area of the forest at any observation point above the soil.

$$\bar{\mathbf{E}}^s(\bar{\mathbf{r}}) = \bar{\mathbf{E}}_{\text{Sb}}^s(\bar{\mathbf{r}}) + \bar{\mathbf{E}}_{\text{Db}}^s(\bar{\mathbf{r}}) + \bar{\mathbf{E}}_{\text{Tb}}^s(\bar{\mathbf{r}}) \quad (8)$$

Thus, it is possible to analyze the relative contribution of each scattering mechanism to the scattered field as in [3].

3. THE INDOOR SCALED-MODEL MEASUREMENTS

Since environmental conditions and experimental uncertainties may dramatically influence the scattering as well as the forest electromagnetic properties change during the year, the underlying idea was to



Figure 2. Photo of the measurement.

carry out bistatic scaled-model measurements in an anechoic chamber. Their aim was to validate our scattering model in well controlled conditions.

All experiments have been conducted in the anechoic chamber of CCRM in Marseille, France. The dimensions of the anechoic chamber are equal to $14 \times 6.5 \times 6.5 \text{ m}^3$. The bistatic measurement setup consists of two antennas, a transmitter and a receiver, placed on an semi-circular vertical arch and a rotating arm, a network analyzer, synthesizers and external mixers. Furthermore, a vector network analyzer (Agilent HP 8510), which was used in a multiple sources configuration with two synthesizers and two external mixers (the measured noise floor level is about -100 dB and the dynamic range is equal to 89 dB) is used to measure the amplitude and the phase of the electric fields. In this study, we use two types of transmitting antennas: a parabolic one (Hyptra NE5256) which operates in C-band ($4\text{--}8 \text{ GHz}$) and a horn antenna that operates in X-band ($8\text{--}12 \text{ GHz}$). The receiving antenna is a wide band ridged horn antenna (ARA DRG-118) with a frequency range of 1 to 18 GHz.

To perform measurements of the scattered fields by the scale models of the forest, we began by attaching the aluminum circular plate that models the forest ground on the ceiling of the anechoic chamber by metallic cables (see Figure 2). The plate is thus placed in a horizontal plane and such as its center coincides with setup center. Besides, the plate is surrounded by absorbing material to reduce edge effects.

3.1. The Geometric Configurations of Antennas

In our study, we consider two different geometric configurations of antennas representing two special cases of bistatism. The first case is an azimuthal bistatic configuration where the transmitting antenna is

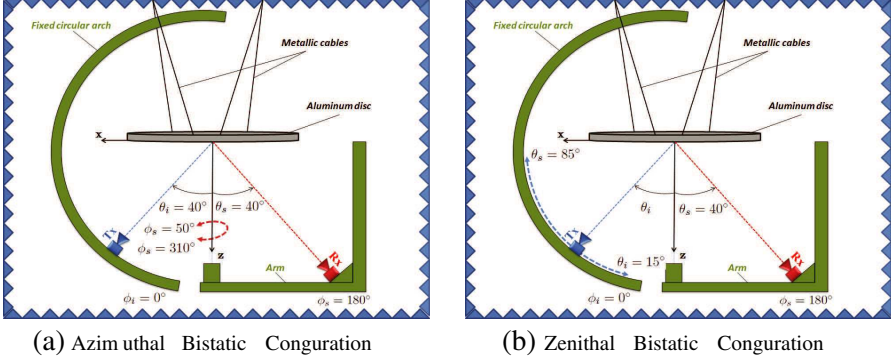


Figure 3. Schematic of the measurement.

fixed on the vertical arch at the position corresponding to the incidence angles ($\theta_i = 40^\circ$, $\phi_i = 0^\circ$). The receiving antenna is placed on an arm such as the zenithal reception angle $\theta_s = 40^\circ$. The arm can be rotated in azimuth around the vertical (z -axis). For this configuration, the electric fields are measured at 131 points describing a circular path with a radius of 2 m (movement of the arm) corresponding to azimuthal reception angles, ϕ_s , from 50° to 310° with an angular step of 2° . The other azimuthal reception angles are not investigated because of physical dimensions of the arch. The azimuthal bistatic configuration is shown schematically in Figure 3(a). In the second case which represents the zenithal bistatic configuration, the transmitter is moved on the semi-circular arch in the xOz -plane ($\phi_i = 0^\circ$) from $\theta_i = 15^\circ$ to $\theta_i = 85^\circ$ with an angular step of 1° (71 incidence positions). In this case, the receiver is fixed on the arm with a zenithal reception angle $\theta_s = 40^\circ$, in the half-plane $\phi_s = 180^\circ$. Therefore, incidence and reception planes are merged. The setup is shown schematically in Figure 3(b). In this configuration, simulations are done considering the reciprocity theorem (reversing source and receiver roles). The equivalent configuration considers a transmitting antenna fixed on the arm as $\theta_i = 40^\circ$ and $\phi_i = 180^\circ$ and a receiver moving on the arch ($\phi_s = 0^\circ$) from $\theta_s = 15^\circ$ to $\theta_s = 85^\circ$ with an angular step of 1° .

3.2. Description of the Forest Scale Models

The forest scale models are made of an aluminium circular plate and targets composed of vertical and/or tilted dielectric parallelepipeds. The targets under study have been chosen to be representative of tree-trunks and main branches at VHF frequencies. They have been glued manually on a circular plate of diameter equal to 90 cm. The plate

was chosen so that all interactions between the target and the plate are taken into account. The plate is maintained to the ceiling of the anechoic chamber by using metallic cables in order to obtain a zenithal reception angle θ_s equal to 40° .

Table 1. Parameters in real and scaled cases.

Parameter	Scaled case	Real case
Trunk's height	7.5 cm	3 m
Trunk's side length	0.75 cm	30 cm
Branch's height	2.5 cm	1 m
Branch's side length	0.5 cm	20 cm
Permittivity	$9 + 0.001 \times j$	$9 + 0.001 \times j$
Distance from plate center to receiver	2 m	80 m
Frequency band	4–12 GHz	100–300 MHz
Frequency step	200 MHz	5 MHz

Table 1 shows the parameters of tree-trunks and branches as well as the investigated frequency band for both real and scaled cases. In this work, we investigate three targets as illustrated in Figure 4.

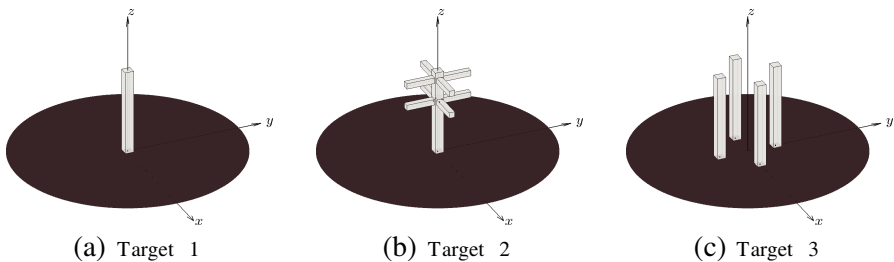


Figure 4. Targets configuration.

Target 1 is a single vertical scaled tree-trunk located at the center of the plate and target 2 represents one scaled tree made of one vertical trunk and 8 horizontally tilted branches. The branches are regularly distributed in azimuth and are located at 4.75 and 6.75 cm from the plate. Finally, target 3 is composed of 4 vertical scaled tree-trunks. The distance between each trunk and the plate center is equal to 2.5 cm.

3.3. Measurement Steps and Calibration Procedure

In order to determine the field scattered by each target, we have performed two measurements: first, a measurement of the total field (the field in the presence of the targets on the circular plate) and second a measurement of the reference field (the field measured without any target on the circular plate). The reference field is then coherently subtracted from the total field to obtain the scattered field. It is important to underline that during positioning of the targets, the plate can be involuntarily slightly tilted. Hence, we have chosen to measure the total field before the reference field in order to minimise measurement errors due to the moving of the plate.

In addition, the reference and total field measurements are not performed at the same time and they require up to several hours. During this time, drift phenomena due to time as temperature are occurring. The drift correction presented in [22] was applied to scattered electric field to increase the measurement accuracy.

To reference the module and phase of the experimental scattered field, a calibration using a reference target was applied [23]. The theoretical scattered field of the reference target must be accurately known. Several canonical shapes, including metal disks and rectangular plates, have scattered fields known with a high degree of accuracy in the specular direction [3]. We have chosen a dielectric cube of dimensions equal to $40 \times 40 \times 40 \text{ mm}^3$ and relative permittivity 2.35 which is positioned at the center of the plate. This calibration procedure provides a complex coefficient for each frequency, C_f , to minimize the difference between the theoretical and experimental scattered fields of the dielectric cube. In our case, this coefficient normalizes the amplitude of the incident field to the unity (1 V/m) and its phase to zero at the center of the plate. This procedure is essential to compare qualitatively measurement results with those of the simulation.

We have chosen the azimuthal bistatic configuration and the HH -polarisation to compute the calibration coefficient by using the following formula:

$$C_f = \frac{\sum_{\phi_s} \bar{\mathbf{E}}_{\text{sim}}^s \text{conj}(\bar{\mathbf{E}}_{\text{meas}}^s)}{\sum_{\phi_s} |\bar{\mathbf{E}}_{\text{meas}}^s|^2} \quad (9)$$

where $\text{conj}(\bar{\mathbf{E}}_{\text{meas}}^s)$ is the conjugate of the measured scattered field by the cube, $\bar{\mathbf{E}}_{\text{meas}}^s$, and $\bar{\mathbf{E}}_{\text{sim}}^s$ is the theoretical scattered field by the cube.

Finally, we multiply the calibration coefficient by the measured scattered fields of the proposed targets to obtain the calibrated data.

4. THEORETICAL AND EXPERIMENTAL RESULTS

This section is composed of two subsections. In the first subsection, experimental and theoretical fields scattered by the targets, illustrated in Figure 4, are presented and compared. Two important bistatic geometric configurations with a special attention to the specular direction are considered: an azimuthal and a zenithal bistatic configurations. Only VV - and HH -polarized scattered fields have been measured. The second subsection focuses on the contribution of the scattering mechanisms to the full-polarized scattered field by target 3 for both azimuthal and zenithal bistatic configurations.

4.1. Numerical Simulations Compared with Experimental Data

In Figure 5, the experimental and theoretical fields scattered by the target 1 are plotted with respect to the azimuthal reception angle ϕ_s .

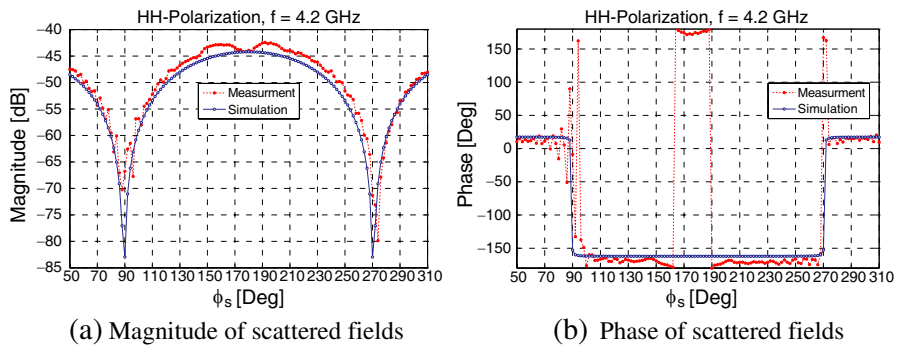


Figure 5. Variation of experimental and theoretical scattered fields by target 1 at $f = 4.2$ GHz with respect to azimuthal reception angle ϕ_s for HH -polarization.

The theoretical and experimental scattered fields are in good agreement (magnitude and phase). The maximum of the theoretical scattered field is obtained in the specular direction ($\theta_s = \theta_i = 40^\circ$, $\phi_s = 180^\circ$). Small oscillations probably due to saturation can be observed near the specular scattering direction that are not present in the computed results. These fluctuations appear in particular for lower magnitude levels of the scattered field which are more sensitive to noise. By analyzing the azimuthal geometric configuration and the target symmetry, a symmetry of the field scattered by the target 1 about the azimuthal reception angle $\phi_s = 180^\circ$ is expected. This symmetry is not

perfect for the experimental scattered field, in particular for the lower magnitude levels which are more sensitive to noise. The dissymmetry can be due to many factors as target position error, target orientation error, receiver position error, plate misalignment.

In Figure 6, we present the magnitude of theoretical and experimental fields scattered by the target 1 versus the zenithal reception angle θ_s for VV -polarization at $f = 8.8$ GHz and HH -polarization at $f = 5.2$ GHz.

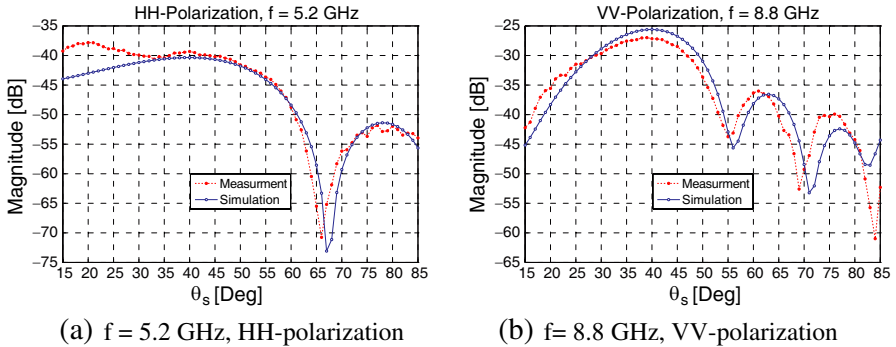


Figure 6. Magnitude of experimental and theoretical scattered fields by target 1 with respect to zenithal reception angle θ_s .

In this case of zenithal geometric configuration, a good agreement between simulations and measurements is obtained for both the VV - and HH -polarizations. Simulated results indicate that highest levels are collected in the specular direction ($\theta_s = \theta_i = 40^\circ$, $\phi_s = 180^\circ$). We can also observe angular shifts between theoretical and experimental plots for VV - and HH -polarizations.

We turn now to study the bistatic scattering by a more complicated target representing one scaled tree composed of one vertical tree-trunk and eight horizontally tilted branches. We are interested here in the azimuthal geometric configuration. Thus, we show in Figure 7 the magnitude as well as the phase of HH -polarized theoretical and experimental scattered fields by target 2 at $f = 9.8$ GHz versus the azimuthal reception angle ϕ_s .

On most observation points, Figure 7 shows that we obtained a good agreement between theoretical and experimental HH -polarized scattered fields. However, a difference in the magnitude of scattered fields is observed in the angular regions from 110° to 130° and from 230° to 250° . In fact, given the complexity of target 2, additional errors, due to the imperfections of the target, can disrupt the measurement. This may introduce the asymmetry on the experimental scattered field

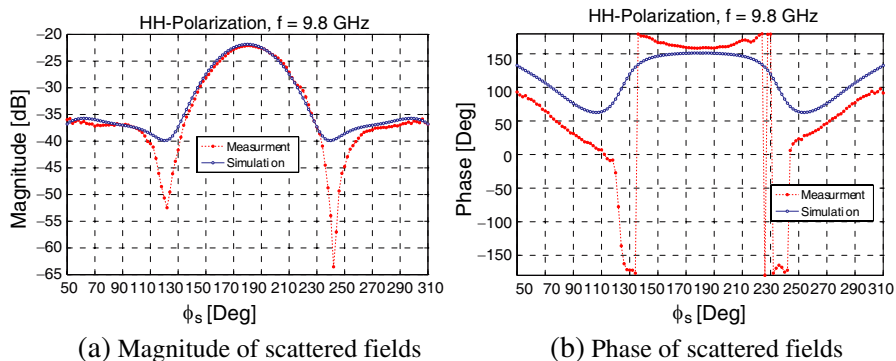


Figure 7. Variation of experimental and theoretical *HH*-polarized scattered fields by target 2 at $f = 9.8$ GHz with respect to azimuthal reception angle ϕ_s .

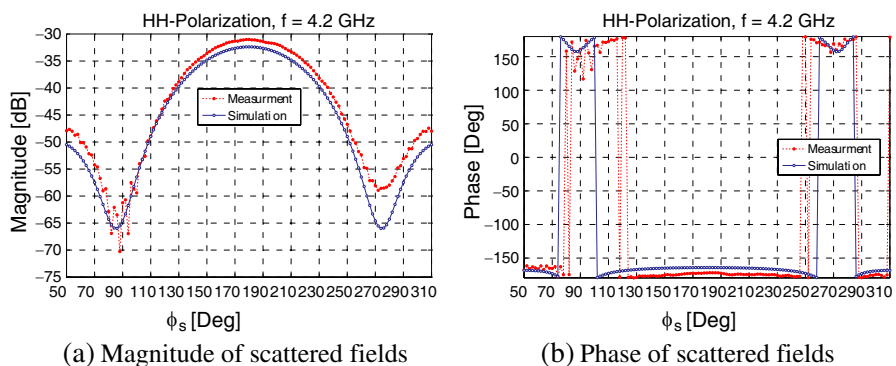


Figure 8. Variation of experimental and theoretical *HH*-polarized scattered fields by target 3 at $f = 4.2$ GHz with respect to azimuthal reception angle ϕ_s .

magnitude observed in Figure 7(a). The lower levels of the scattered fields being once more th most difficult to measure precisely.

Let’s move now on to evaluate the bistatic scattering by the last target (target 3), including four vertical scaled tree-trunks.

We firstly show, in Figure 8, the variation of the *HH*-polarized experimental and theoretical scattered fields by target 3 at $f = 4.2$ GHz versus azimuthal reception angle ϕ_s . This figure indicates that the experimental data are in very good agreement with the simulated results. The maxima of *HH*-polarized theoretical and experimental scattered field are observed in the specular direction

($\theta_s = \theta_i = 40^\circ$, $\phi_s = 180^\circ$). Furthermore, we can see that, conversely to theoretical scattered fields, experimental scattered fields are asymmetric about the incidence plane.

After that, we compare experimental and theoretical HH -polarized scattered fields by the same target at $f = 4.4$ GHz with respect to zenithal reception angle θ_s (see Figure 9).

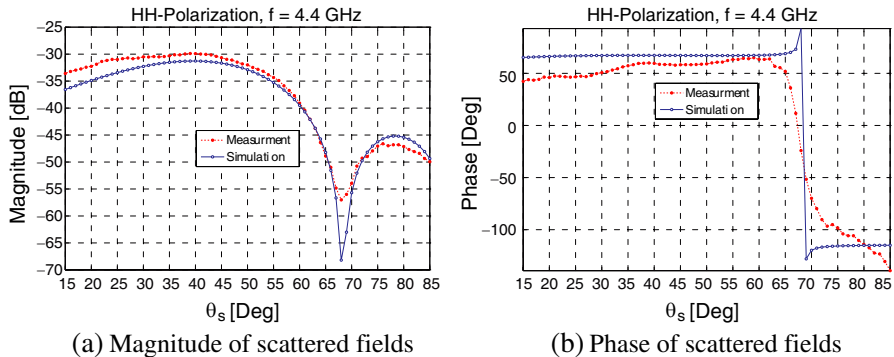


Figure 9. Variation of experimental and theoretical scattered fields by target 3 at $f = 4.4$ GHz with respect to zenithal reception angle θ_s for HH polarization.

For this target, we also obtain a good concordance between simulation and measurement. As it is seen in Figure 9(a), the maxima of the scattered fields are obtained in the specular direction ($\theta_s = 40^\circ$).

4.2. Analysis of the Contributions of Bistatic Scattering Mechanisms

In this subsection, we use the model introduced in Section 2 to evaluate the contribution of the scattering mechanisms to the scattered fields by target 3 at $f = 4.2$ GHz. We consider both azimuthal and zenithal geometric configurations. In the case of the azimuthal geometric configuration, results are plotted for both co- and cross-polarizations.

In contrast, for the zenithal geometric configuration, only co-polarizations results are represented, as cross-polarizations are null due to symmetry reasons. For this configuration, the incidence and the reception planes are the same representing a symmetry plane for the target 3. In Figure 10, we show the contribution of the scattering mechanisms to the fields scattered by target 3 for both co- and cross-polarizations. Figures 10(a) and 10(b) show that the Db is the most important scattering mechanism that contributes to the co-polarized scattered field for all azimuthal reception angles ϕ_s . Moreover, the

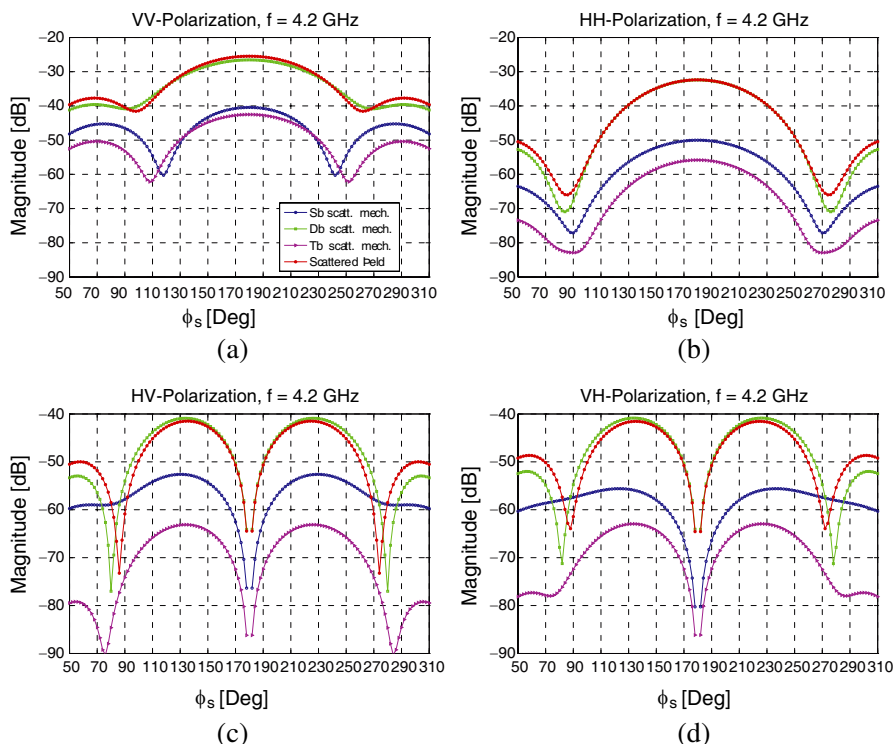


Figure 10. Contribution of the scattering mechanisms to the scattered field by target 3 versus the zenithal reception angle ϕ_s .

contribution of other scattering mechanisms is low. It is important to note that, at specular direction, the *VV*-polarized scattered field level is greater than *HH*-polarized scattered field level. This can be explained by the vertical orientation of the scaled tree-trunks.

Figures 10(c) and 10(d), show that *HV*- and *VH*-polarized scattered fields are null in the specular direction (at $\phi_s = 180^\circ$). In this direction, the incidence and the reception planes are merged and represent a target symmetry plane. We can also see that the cross-polarized scattered fields are mainly due to the Db scattering mechanism. Furthermore, these figures indicate that the behavior of Sb and Tb scattering mechanisms is not the same for *HV*- and *VH*-polarizations. The contribution of the Tb scattering mechanism is negligible with respect to Db scattering mechanism. We note that the cross-polarization returns are not due to target geometry but to changes of the reception plane (bistatism).

With regard to the zenithal geometric configuration, Figure 11

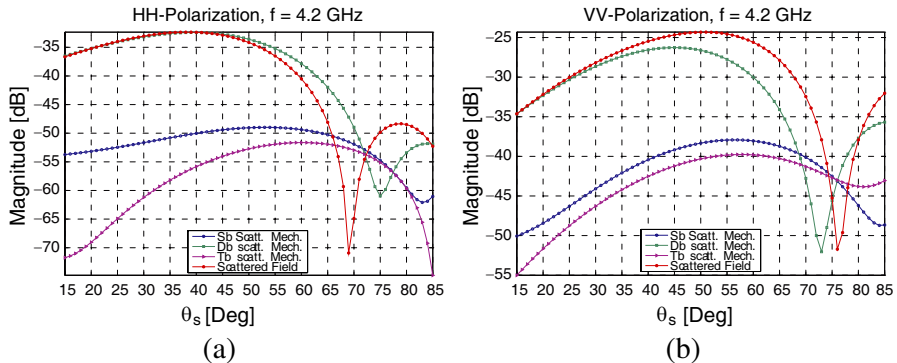


Figure 11. Contribution of the scattering mechanisms to the scattered field by target 3 versus the zenithal reception angle θ_s .

shows the contribution of the scattering mechanisms to the scattered fields by target 3 for both VV - and HH -polarizations versus the zenithal reception angle θ_s . As it can be seen, the Db is the dominant scattering mechanism for a wide range of zenithal reception angles θ_s , except for when $\theta_s \in [72^\circ-77^\circ]$ (HH -polarization) and $\theta_s \in [69^\circ-76^\circ]$ (VV -polarization).

5. CONCLUSION

In this paper, a rigorous bistatic scattering model simulating the interaction of VHF and low-UHF electromagnetic waves with a simplified forest geometry is presented. It is based on an electric field integral equation formulation solved by using a Method of Moments. The model provides in addition to the scattered field, the contributions of the various scattering mechanisms at any observation point above the ground.

Using the anechoic chamber of CCRM, we have performed a set of scaled-model measurements in order to predict the bistatic scattering by forested areas at VHF frequencies. The forest scale models are made of an aluminum circular plate and targets composed of vertical and/or tilted dielectric parallelepipeds representing respectively the tree-trunks and the primary branches. Three targets with different degrees of complexity are studied. Both azimuthal and zenithal geometric configurations are employed to measure the co-polarized scattered fields.

Measurement data have been presented and confronted with numerical simulations. The obtained results are extremely encouraging. We have seen that theoretical and experimental scattered fields are in

good agreement for both the magnitude and phase. The analysis of the results allow us to conclude on problems related generally to the experiment that we are rather confident to be able to solve in the near future. These problems are generally associated with the misalignment, positioning of targets and the circular plate instability. Measurement results allowed us to validate our theoretical model for both VV - and HH -polarizations. The obtained results can be used as a starting point for devising procedures for retrieval of forest parameters and interpreting bistatic SAR images.

We have also analyzed the contribution of the scattering mechanisms to the full-polarized scattered field. To summarize the findings of this study, we have seen that the contribution of the Db scattering mechanism is important compared to the other scattering mechanisms for both the co- and cross-polarizations.

Finally, as a guideline for future work, it is important to measure co- and cross-polarized scattered fields using over more complicated targets.

REFERENCES

1. Krieger, G. and A. Moreira, "Multistatic SAR satellite formations: Potentials and challenges," *International Geoscience and Remote Sensing Symposium*, Vol. 4, 2680, 2005.
2. Krieger, G., H. Fiedler, and A. Moreira, "Bi- and multistatic SAR: Potentials and challenges," *Proc. EUSAR*, Vol. 34, 365–370, 2004.
3. Bradley, C. J., P. J. Collins, J. Fortuny-Guasch, M. L. Hastriter, G. Nesti, A. J. Terzuoli, Jr., and K. S. Wilson, "An investigation of bistatic calibration objects," *IEEE Transactions on Geoscience and Remote Sensing*, Vol. 43, No. 10, 2177–2184, 2005.
4. Glaser, J. I., "Some results in the bistatic radar cross section (RCS) of complex objects," *Proceedings of the IEEE*, Vol. 77, 639–648, 2002.
5. Dubois-Fernandez, P., H. Cantalloube, B. Vaizan, G. Krieger, R. Horn, M. Wendler, and V. Giroux, "ONERA-DLR bistatic SAR campaign: Planning, data acquisition, and first analysis of bistatic scattering behaviour of natural and urban targets," *IEE Proceedings. Radar, Sonar and Navigation*, Vol. 153, 214, 2006.
6. McLaughlin, D. J., Y. Wu, W. G. Stevens, X. Zhang, M. J. Sowa, and B. Weijers, "Fully polarimetric bistatic radar scattering behavior of forested hills," *IEE Proceedings. Radar, Sonar and Navigation*, Vol. 50, 101–110, 2002.

7. Liang, P., L. E. Pierce, and M. Moghaddam, "Radiative transfer model for microwave bistatic scattering from forest canopies," *IEEE Transactions on Geoscience and Remote Sensing*, Vol. 43, 2470–2483, 2005.
8. Thirion-Lefevre, L., E. Colin-Koeniguer, and C. Dahon, "Bistatic scattering from forest components. Part I: Coherent polarimetric modelling and analysis of simulated results," *Waves in Random and Complex Media*, Vol. 20, 36–61, 2010.
9. Nguyen, H., H. Roussel, and W. Tabbara, "A coherent model of forest scattering and SAR imaging in the VHF and UHF band," *IEEE Transactions on Geoscience and Remote Sensing*, Vol. 44, 838–848, 2006.
10. Oh, Y., Y. M. Jang, and K. Sarabandi, "Full-wave analysis of microwave scattering from short vegetation: An investigation on the effect of multiple scattering," *IEEE Transactions on Geoscience and Remote Sensing*, Vol. 40, 2522–2526, 2003.
11. Israelsson, H., L. M. H. Ulander, T. Martin, and J. I. H. Askne, "A coherent scattering model to determine forest backscattering in the VHF-band," *IEEE Transactions on Geoscience and Remote Sensing*, Vol. 38, 238–248, 2002.
12. Eigel, R. L., P. J. Collins, A. J. Terzuoli, G. Nesti, and J. Fortuny, "Bistatic scattering characterization of complex objects," *IEEE Transactions on Geoscience and Remote Sensing*, Vol. 38, 2078–2092, 2000.
13. Ulaby, F. T., T. E. van Deventer, J. R. East, T. F. Haddock, and M. E. Coluzzi, "Millimeter-wave bistatic scattering from ground and vegetation targets," *IEEE Transactions on Geoscience and Remote Sensing*, Vol. 26, 229–243, 2002.
14. Hauck, B., F. Ulaby, and R. DeRoo, "Polarimetric bistatic-measurement facility for point and distributed targets," *IEEE Antennas and Propagation Magazine*, Vol. 40, 31–41, 2002.
15. Eyraud, C., J. M. Geffrin, P. Sabouroux, P. C. Chaumet, H. Tortel, H. Giovannini, and A. Litman, "Validation of a 3D bistatic microwave scattering measurement setup," *Radio Science*, Vol. 43, 1992–2005, 2008.
16. Gürel, L., H. Bağcı, J. C. Castelli, A. Cheraly, and F. Tardivel, "Validation through comparison: Measurement and calculation of the bistatic radar cross section of a stealth target," *Radio Science*, Vol. 38, 1046, 2003.
17. Sarabandi, K. and A. Nashashibi, "A novel bistatic scattering matrix measurement technique using a monostatic radar," *IEEE Transactions on Antennas and Propagation*, Vol. 44, 41–50, 2002.

18. Ziade, Y., H. Roussel, M. Lesturgie, and W. Tabbara, "A coherent model of forest propagation — Application to detection and localization of targets using the DORT method," *IEEE Transactions on Antennas and Propagation*, Vol. 56, 1048–1057, 2008.
19. Colin-Koeniguer, E. and L. Thirion-Lefevre, "Bistatic scattering from forest components. Part II: First validation of a bistatic polarimetric forest model in the VHF-UHF band [225–475 MHz] using indoor measurements," *Waves in Random and Complex Media*, Vol. 20, 62–85, 2010.
20. Bellez, S., C. Dahon, and H. Roussel, "Analysis of the main scattering mechanisms in forested areas: An integral representation approach for monostatic radar configurations," *IEEE Transactions on Geoscience and Remote Sensing*, Vol. 47, 4153–4166, 2009.
21. Hunka, J., R. Stovall, and D. Angelakos, "A technique for the rapid measurement of bistatic radar cross sections," *IEEE Transactions on Antennas and Propagation*, Vol. 25, 243–248, 2002.
22. Eyraud, C., J. M. Geffrin, A. Litman, P. Sabouroux, and H. Giovannini, "Drift correction for scattering measurements," *Applied Physics Letters*, Vol. 89, 244104, 2006.
23. Merchiers, O., C. Eyraud, J. M. Geffrin, R. Vaillon, B. Stout, P. Sabouroux, and B. Lacroix, "Microwave measurements of the full amplitude scattering matrix of a complex aggregate: A database for the assessment of light scattering codes," *Opt. Express*, Vol. 18, 2056–2075, 2010.